THE BACKGROUND EMISSION ANISOTROPY SCANNING TELESCOPE (BEAST) INSTRUMENT DESCRIPTION AND PERFORMANCES

JEFFERY CHILDERS,[1] MARCO BERSANELLI,[2] NEWTON FIGUEIREDO,[3] TODD C. GAIER,[4] DORON HALEVI,[1] MIIKKA KANGAS,[1] ALAN LEVY,[1] PHILIP M. LUBIN,[1] MARCO MALASPINA,[5] NAZZARENO MANDOLESI,[5] JOSHUA MARVIL,[1] PETER R. MEINHOLD,[1] JORGE MEJÍA,[6] PAOLO NATOLI,[7] HUGH O'NEILL,[1] SHANE PARENDO,[1] MICHAEL D. SEIFFERT,[4] NATHAN C. STEBOR,[1] FABRIZIO VILLA,[5] THYRSO VILLELA,[6] BRIAN WILLIAMS,[1] AND CARLOS ALEXANDRE WUENSCHE[6]

ABSTRACT

The Background Emission Anisotropy Scanning Telescope (BEAST) is a millimeter wavelength experiment designed to generate maps of fluctuations in the cosmic microwave background (CMB). The telescope is composed of an off-axis Gregorian optical system with a 2.2 m primary that focuses the collected microwave radiation onto an array of cryogenically cooled high electron mobility transistor (HEMT) receivers. This array is composed of six corrugated scalar feed horns in the Q band (38 to 45 GHz) and two more in the Ka band (26 to 36 GHz) with one of the six Q-band horns connected to an ortho-mode transducer for extraction of both polarizations incident on the single feed. The system has a minimum beam size of $20'$ with an average sensitivity of $900\ \mu K\ \sqrt{s}$ per receiver. This paper describes the design and performance of the BEAST instrument and provides the details of subsystems developed and used toward the goal of generating a map of CMB fluctuations on $20'$ scales with sensitivity in l space between $l \sim 100$ and $l \sim 500$. A map of the CMB centered on the north celestial pole has been generated from the BEAST telescope in a $9°$ wide annulus at declination $37°$ with a typical pixel error of $57 \pm 5\ \mu K$ when smoothed to $30'$ resolution. A brief summary of the map and results generated by an observing campaign at the University of California White Mountain Research Station are also included.

Subject heading: cosmology: observations

Online material: color figures

1. INTRODUCTION

One of the primary goals of modern cosmology is the determination of fundamental cosmological parameters. One of the few relics remaining today that allow this determination is the cosmic microwave background (CMB). Anisotropies, or temperature fluctuations, exist in the CMB that reflect the morphology of matter at the time of the recombination of electrons with nuclei, which occurred at a redshift $z \sim 1100$ (Peebles 1993). By careful measurement of the angular power spectrum of anisotropies in the CMB, we can extract fundamental parameters encoded in the structure of the anisotropies (Kolb & Turner 1990). This paper describes a microwave telescope that is intended to measure portions of the microwave sky in order to estimate the angular power spectrum of the CMB in the approximate range of a few degrees down to $0°.15$ ($l \sim 100–500$). The target cosmological parameters to be extracted from this region of the angular power spectrum are Ω_0, the total matter density of the universe; Ω_B, the matter density in baryons; H_0, Hubble's constant; and λ, the cosmological constant.

The telescope, named the Background Emission Anisotropy Scanning Telescope (BEAST), houses an off-axis Gregorian optical system, the key feature of which is a 2.2 m primary reflector and 0.9 m secondary reflector terminating on a HEMT-based array of cryogenic detectors, which operate in the Q band as well as the Ka band. The receivers operate in total power mode, with modulation on the sky achieved through the use of a rotating flat reflector. An important advantage of this instrument concept is the intrinsic simplicity of the receiver and the better intrinsic sensitivity (factor of $\sqrt{2}$) due to the nonswitching scheme. The telescope is built into a stabilized platform that was originally designed to collect data at ~ 35 km altitude during either continental (short-duration) or circumpolar LDB (long-duration) balloon flights. BEAST flew twice as a balloon-borne instrument in May and October of 2000 and then was reconfigured to observe as a ground-based instrument for use at a high-altitude site (3875 m) at the White Mountain Research Station in California.

1.1. Optics

The optical system employed on the BEAST telescope (see Table 1) is based on an off-axis Gregorian configuration obeying the Dragone-Mizuguchi condition (Dragone 1978; Mizuguchi et al. 1978). The primary reflector (the largest flown on a stabilized balloon platform) is a 2.2 m off-axis parabolic reflector that receives its input beam from a rotating flat reflector of 2.6 m in diameter. The surface of this flat reflector is tilted by $2°.2$ with respect its rotation axis. The result is that, as the flat is rotated, the optical beam is directed along an approximately elliptical path on the sky. In the data analysis, the elliptical path is "cut" into 250 equal segments (called flat sectors), each of which corresponds to a specific physical orientation of the rotating flat

[1] Physics Department, University of California, Santa Barbara, CA 93106.
[2] Physics Department, University of Milano, via Celoria 16, 20133 Milano, Italy.
[3] Universidade Federal de Itajubá, Departamento de Física e Química, Caixa Postal 50 37500-903, Itajubá, MG, Brazil.
[4] Jet Propulsion Laboratory, California Institute of Technology, Oak Grove Drive, Pasadena, CA 91109.
[5] Dipartimento di Fisica e sezione INFN, Università di Roma "Tor Vergata," Rome, Italy.
[6] Instituto Nacional de Pesquisas Espaciais, Divisão de Astrofísica, Caixa Postal 515, 12210-070, São José dos Campos, SP, Brazil.
[7] IFP-CNR, via Cozzi 53, 20125 Milano, Italy.

TABLE 1
PHYSICAL PARAMETERS OF MAJOR ELEMENTS OF THE OPTICAL SYSTEM

Parameter	Value
Primary Reflector	
Focal length, OVp	1250.0 mm
Maximum physical dimension, AC	2200.0 mm
Minimum physical dimension	1966.1 mm
Secondary Reflector	
Semimajor axis of parent ellipsoid...............................	886.7 mm
Semiminor axis of parent ellipsoid	853.4 mm
Focal length, f..	240.7 mm
Eccentricity, e..	0.2714
Flat Reflector	
Diameter, KM	2600.0 mm
Telescope	
Feed angle..	58°.2
Angle between axes of parent figures.........................	35°.4

FIG. 1.—Layout of the Gregorian optical system utilized by BEAST telescope on a cut through the symmetry (y, z) plane. The units are mm, with the origin placed at the focal point shared between the primary and secondary reflectors. The geometric optical lines are depicted in blue. The flat, the primary (along with its parent parabola), the secondary (with its parent ellipsoid), and the Dewar are shown. The geometric optical lines are sourced from the sky as they approach the flat reflector. [*See the electronic edition of the Supplement for a color version of this figure.*]

reflector. The incoming radiation is reflected off of the primary toward the secondary reflector with which it shares a focus. The 0.9 m ellipsoidal secondary reflects the incoming radiation toward the array of scalar feed horns that couple the radiation to the array of cryogenic low-noise amplifiers (LNAs). A diagram showing the major elements of the optical system is given in Figure 1. This image is a cut through the plane of symmetry of the optical system.

The receiver array is shown in Figure 2. Each feed horn is tilted by several degrees with respect to the others to minimize distortions. The position of each feed places the beam for a particular receiver at a slightly different location on the sky. As the flat rotates, each of these beams follows a separate elliptical path with a characteristic angular size of 8°.8 for any particular detector element. The collection of approximate beam paths for all elements in the array is shown in Figure 3. In this figure, the beam paths are shown for all eight beams (6 Q band and 2 Ka band). While scanning along the elliptical paths generated by the optical system, each receiver produces a variable offset as a result of the changing air mass viewed by the beam. Since the data, before analysis, is naturally separated into ~55 minute intervals as a result of the hourly calibration sequence (described below), we remove the variable offset by generating an hourly template that is removed from the data before further analysis. In addition, we high-pass the data stream at 10 Hz to effectively remove not only the atmospheric offset, but also any spin-synchronous offset associated with the data acquisition. These steps are described in detail in Meinhold et al. (2005). The flat reflector is rotated at approximately 5 Hz for balloon-based data acquisition and 2 Hz for ground-based data acquisition owing to atmospheric drag. A detailed description of the BEAST optical system design is given in Figueiredo et al. (2005), and the reconstruction of the beam paths on the sky from the orientation and positions of the optical elements is covered in Staren (1999) and Natoli (1998).

The BEAST experiment has an inherent sensitivity to the modes of spherical harmonic decomposition of the CMB temperature fluctuations in our map, described by a window function. This sensitivity is based on the characteristics of the instrument, the scanning strategy, and the region of the sky that is sampled.
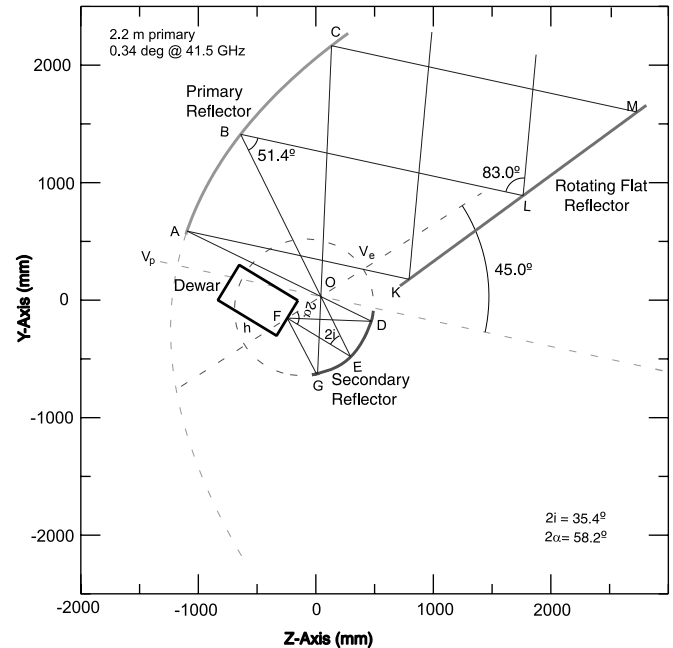
Our window function has a high-frequency roll-off due to our finite beam size; clearly, we cannot discriminate power at angular scales much less than the angular scale of our beam. On the low-frequency side we have two elements that fold together to generate an opposing limit: the 10° chop is one element, and the fraction of sky plus geometry of the final map is the other. The experimental window function, modulo the effects of incomplete sky coverage, are presented in Meinhold et al. (2005). The power spectrum analysis of the resulting map is performed using the MASTER method (Wandelt et al. 2001; Hivon et al. 2002), and the window function (referred to as the transfer function) is calculated using Monte Carlo analysis and presented in O'Dwyer et al. (2005).

Both the primary and secondary reflectors used in this optical system were manufactured from lightweight carbon fiber rather than being machined directly from aluminum. Once complete, they were coated with ~2.6 μm of aluminum to enhance reflectivity, and then with ~0.2 μm of SiO$_x$ to prevent oxidation. The final reflectivity for each surface was not measured. Although the process is more expensive during the first manufacture cycle, the production of a mandrel (the "negative" of the desired reflector surface) allows high-precision and low-cost replication of the original surface for successive builds. For both the primary and secondary reflectors, the backing structure, the fabric, and the orientation of the fibers was engineered to ensure negligible effects of thermal expansion in the final products (Pryor 1998). The mandrels used for the manufacture of both the primary and secondary reflector have resulted in optical surface accuracies of 20 and 12 μm, respectively, as measured on a coordinate measuring machine. Figures 4 and 5 show the resulting errors of the desired surface for the primary and secondary reflectors, respectively, with the projection of the backing structures of each reflector superimposed. Clearly visible on the primary reflector
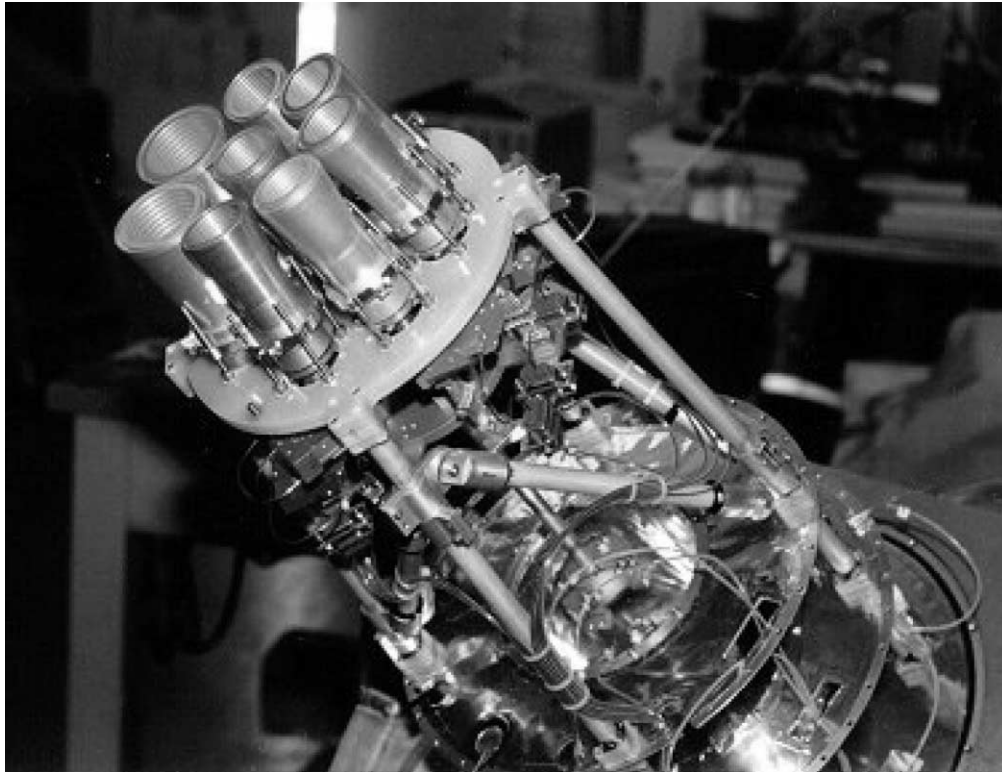
Fig. 2.—Array of BEAST receivers fronted by corrugated scalar feed horns. Each horn is tilted by several degrees with respect to adjacent horns. [*See the electronic edition of the Supplement for a color version of this figure.*]

are deviations on the surface due to this backing structure. The backing structure does not show through very much onto the surface of the secondary, since the cell size of the backing structure is smaller.

BEAST is an alt-az system. The telescope is mounted to an "inner frame" that rotates on two radial bearings driven by a linear actuator. The orientation of the beam and inner and outer frames during sky viewing are shown in Figure 6. After the installation and proper alignment of the reflectors into the mounting structure, the characteristics of the optical response were measured in order to extract the main-beam as well as the sidelobe response
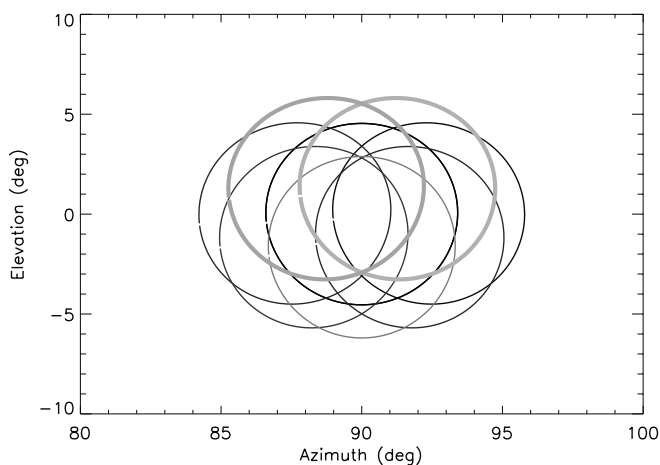
Fig. 3.—Fiducial beam paths of the eight feeds in the BEAST optical array plotted in azimuth (*horizontal*) and elevation (*vertical*) with the centroid fixed at Az = 90° and El = 0. The heavy lines on the "top" of the plot are Ka band, and the rest are Q band. [*See the electronic edition of the Supplement for a color version of this figure.*]

and to verify their consistency with the optical design. The main-beam response was obtained from a measurement of the telescope response when pointing to the Moon. Since the angular size of the Moon is larger than our beam, the main lobe must be deconvolved from the measured telescope response. This is covered in detail in Natoli (1998), and the result for the central Q-band receiver is shown in Figure 7. It is important to note that the plot of the response of the receiver against the distance from the center of the Moon is slightly less than 30′. This is true because the microwave brightness in the model used for the analysis dominates near the center of the Moon, rather than being uniformly distributed across the disk. Another notable feature is the high-frequency structure superimposed on the nearly Gaussian beam pattern resulting from our elliptical scanning strategy combined with the AC decay associated with the data acquisition system (described below). In this case, the design for the main-lobe FWHM was 19′, while the measured main lobe extracted from the Moon data, assumed Gaussian, is 20′ ± 2′, in good agreement with the optical design, and demonstrating that the optics were aligned correctly. Analysis of the resulting map from our data set (Meinhold et al. 2005) demonstrates a nearly symmetric Gaussian beam with an effective FWHM of 22′ rather than the 20′ extracted from the Moon data. The effects that increase the beam FWHM are discussed in the pointing reconstruction section below.

The optical sidelobe response was obtained by measuring the telescope response to a Gunn diode source. The Gunn diode source used for this measurement was placed approximately 50 m away at ~35° elevation on an adjacent building. When placed at this relative position, the source is not in the far field, but near-field effects are not as important for sidelobe response. The telescope was then smoothly scanned across the Gunn diode source and the results for the central receiver (Q band) are shown in Figure 8. The data demonstrate good sidelobe rejection, as expected
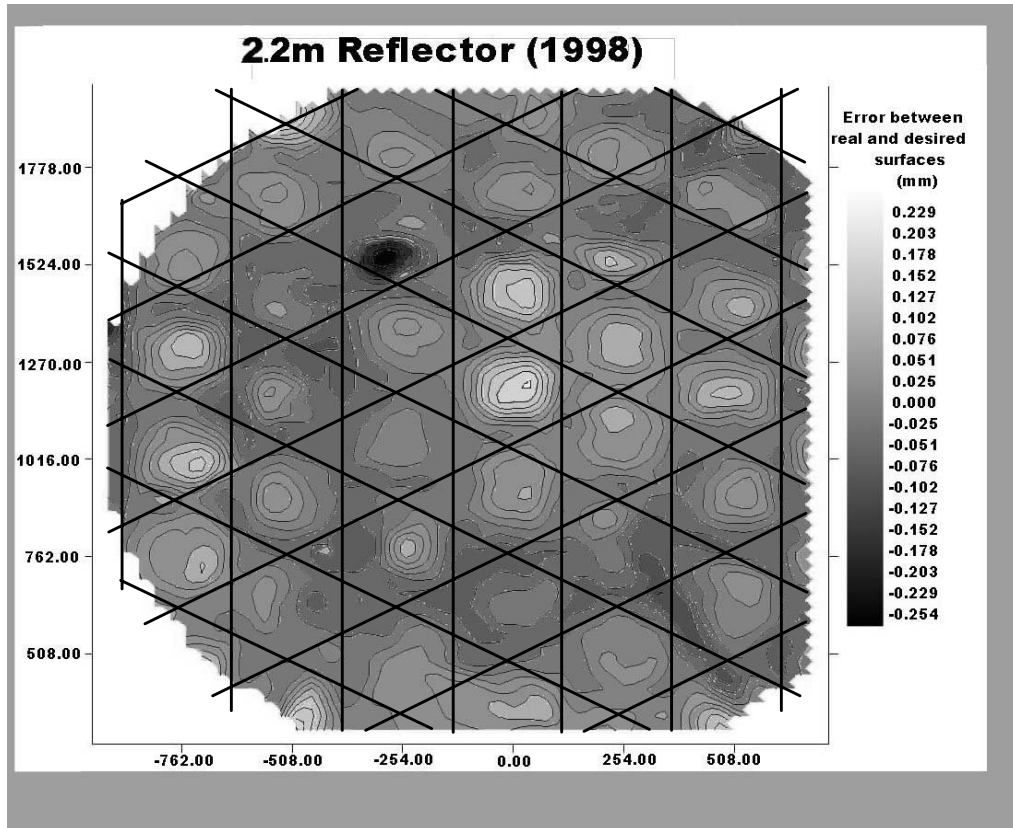
Fɪɢ. 4.—Error plot of primary reflector used for all BEAST campaigns with backing structure superimposed. Deviations from the desired surface due to the large cell size of the backing structure are clearly visible. The 2.2 m parabolic reflector has 20 μm rms error from the desired surface.
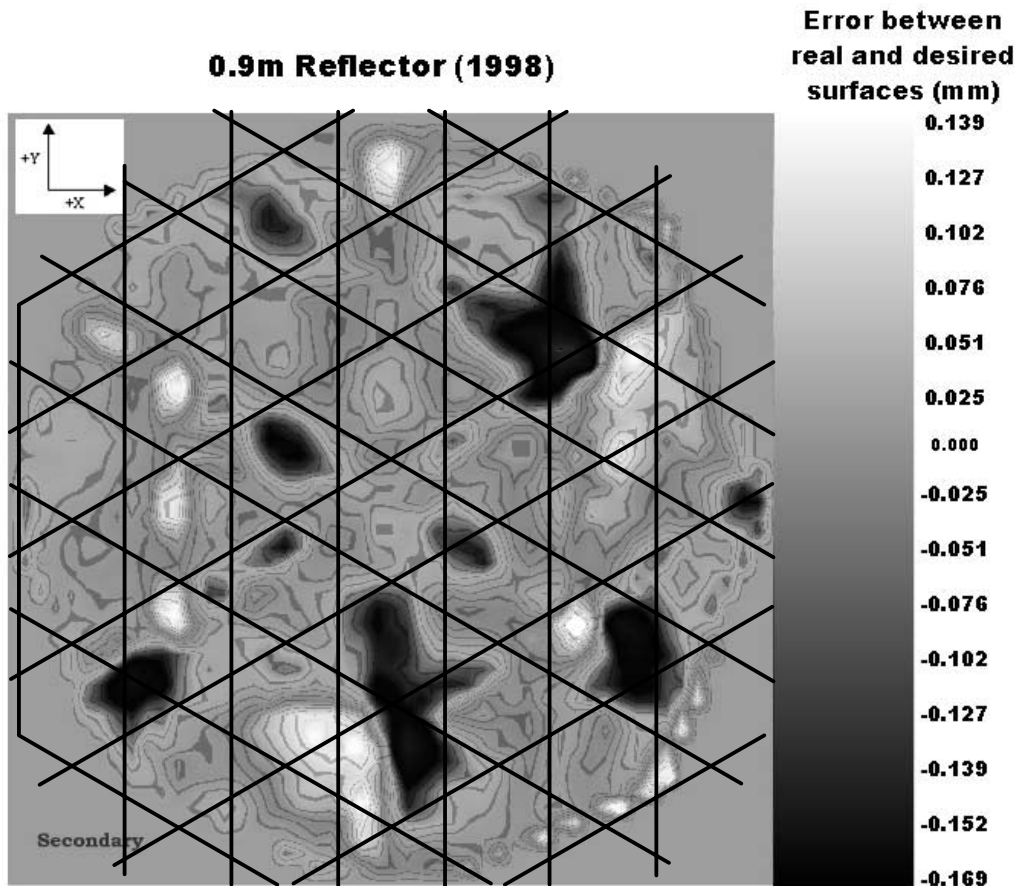

Fɪɢ. 5.—Measured error plot of secondary reflector used for all BEAST campaigns with backing structure superimposed. The 0.9 m secondary reflector has approximately 12 μm rms error from the desired surface.
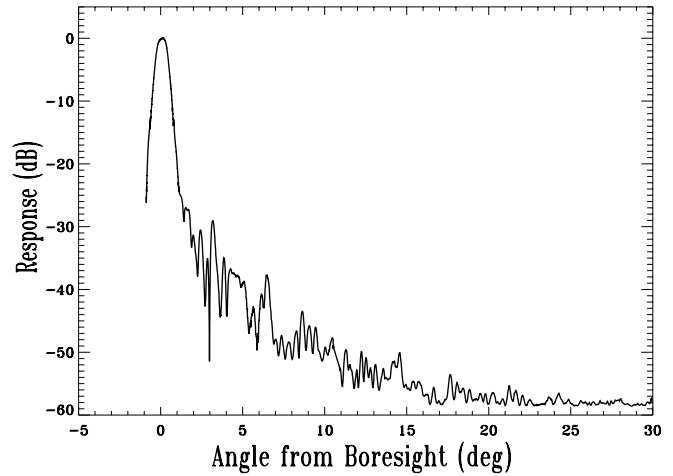
CHILDERS ET AL.

Fig. 8.—Sidelobe response of the central Q-band receiver of the BEAST array installed in the telescope. The telescope minimum sensitivity occurs at −60 dB, so the sidelobe response at angles greater than 20° should be regarded as an upper limit.
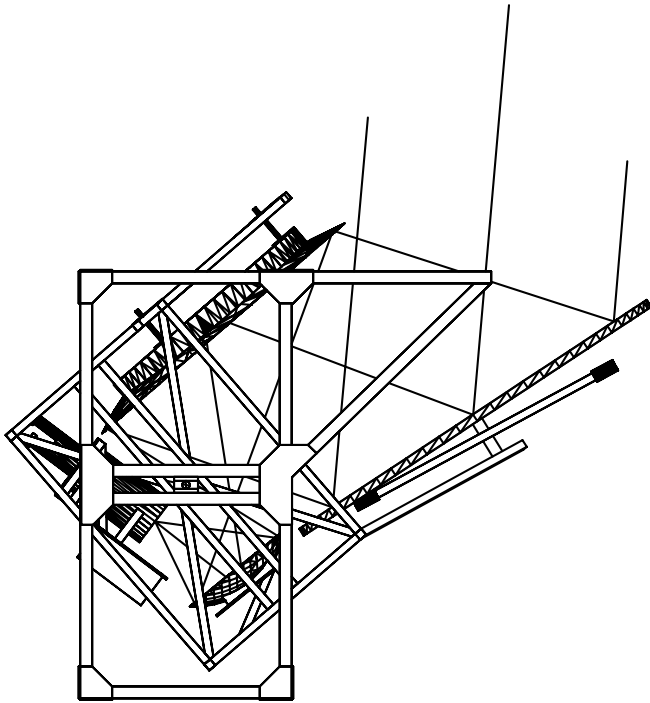
Fig. 6.—Mechanical drawing of BEAST telescope in the orientation used for sky observation at White Mountain. Geometric optical rays are shown as incident vertical lines.

from the optical design, baffling, and the underillumination of our optics (the effective aperture is 1 m in diameter). As shown in Figure 8, at approximately 20° from boresight, the sidelobe response reaches −60 dB, which is the minimum sensitivity for our detector, so the actual response should fall below −60 dB at larger angles.

1.2. Pointing Reconstruction

The most direct product of the BEAST experiment is a map of temperature fluctuations that is generated from the time-ordered
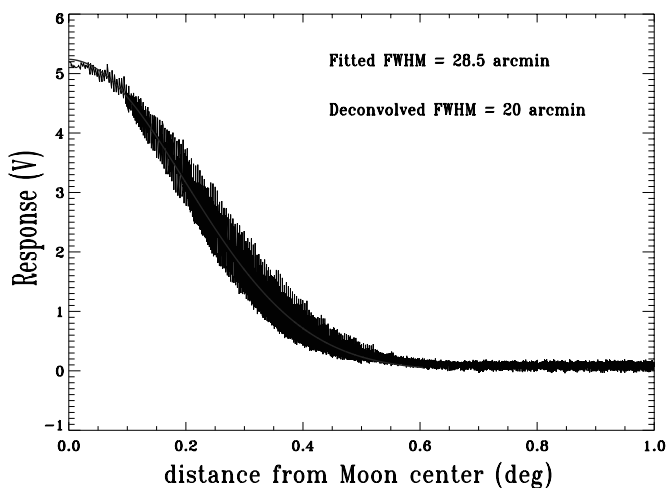
Fig. 7.—Beam response of central element of receiver array to Moon. Beam size is deconvolved from this response, since Moon is not "pointlike," giving deconvolved FWHM of $20' \pm 2'$. The high-frequency structure superimposed on the nearly Gaussian beam pattern is due to our elliptical scanning strategy combined with the AC decay associated with the data acquisition system (adapted from Natoli 1998). [*See the electronic edition of the Supplement for a color version of this figure.*]

data (TOD) collected as the beams are directed at different positions on the sky according to the scanning strategy. The generation of the CMB map from the TOD can only be performed if detailed knowledge of the position of the beam on the sky is well understood for each data point and also for each element in the detector array. Typically, a set of pointing reconstruction elements are attached to the telescope with the purpose of reading out the orientation information required for pointing reconstruction.

For the BEAST telescope at the WMRS Barcroft Station, the only four pieces of information available for any given sky data point are the absolute time, azimuth, and elevation of the centroid of the flat, and the flat sector for each data point. However, the tilt angle of the flat reflector as well as the orientation of both primary, secondary, and each of the corrugated scalar feed horns also are required for pointing reconstruction. To determine these, the telescope must view a celestial source while in the exact configuration as that used for data acquisition. The telescope could not fit through the door of the retrofitted garage at Barcroft Station while assembled and no planets become visible from our observation point in the garage. However, the daily scan of the BEAST telescope crosses the Galactic plane twice, so radio sources that are strong enough to be used for pointing reconstruction were utilized. These radio sources were selected from a Galactic plane survey (Langston et al. 2000) with high signal-to-noise in our map and chosen to avoid confusion during pointing reconstruction. The final determination of these tilt parameters occurred in two steps: coarse determination using an airplane, and fine determination using the radio sources in the Galactic plane.

We began with an approximate set of tilt parameters for the optical elements in both the reflecting optical surfaces and the feed horns in the receiver array. In order to roughly determine these tilt parameters we flew an airplane within the solid angle viewed by the BEAST telescope once the telescope was assembled in its housing at the WMRS. The airplane was equipped with a global positioning system (GPS) in order to track the airplane's longitude, latitude, and altitude versus the GPS time. This information allowed the determination of the absolute position of the airplane in the two-dimensional space viewed by the telescope. Simultaneously, the data acquired by the BEAST telescope viewing the airplane were "stamped" with the same
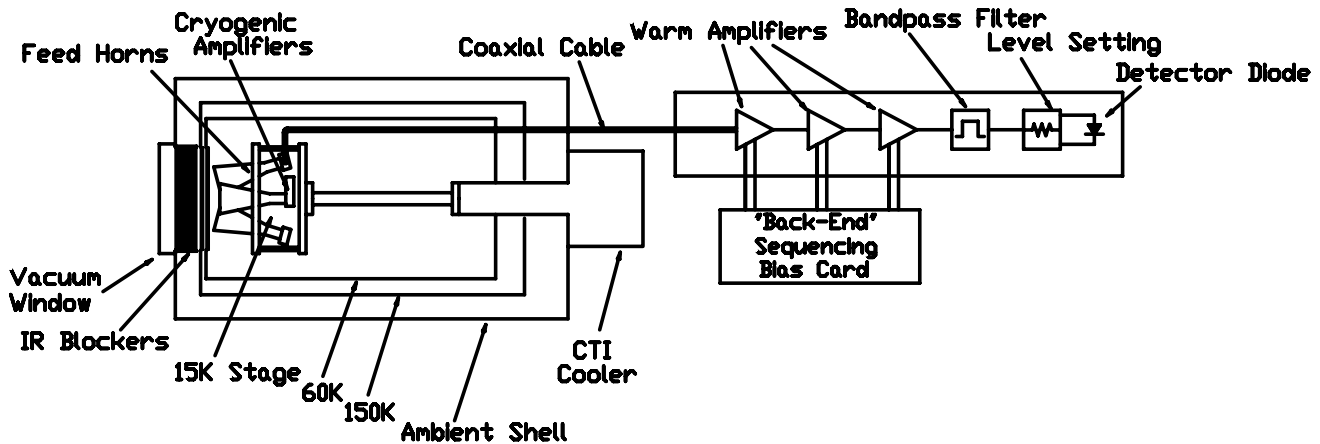
FIG. 9.—Conceptual diagram of BEAST radiometer. CMB radiation enters through the vacuum window terminating into scalar feed horns. Cryogenic low-noise amplifiers boost signal, which is then sent to warm amplification stages via coaxial cable. After warm amplification, the bandpass is defined and signal level is adjusted before termination onto the detector diode.

GPS time as the airplane. Knowing the orientation and position of the telescope then allowed determination of the tilt parameters with an accuracy of $\sim0°.3$. This was only a coarse determination, since the airplane at its distance could not be considered a pointlike object. The final set of tilt parameters was extracted from actual sky data acquired during the observing campaign at the WMRS. By knowing the position of several Galactic point sources at the time of their crossings, and knowing the orientation of the telescope in the garage, we were able to calculate the position of the point source from the telescope point of view at the time they cross the beam. By small adjustments of the optical tilt parameters, we were able to generate a model of the optical system that provides observations that are consistent with the actual positions of the point sources.

The main limitation to accuracy in our pointing reconstruction is due to the data acquisition and subsequent resectoring. As the reflecting flat rotates, the beam is swept along the elliptical path at approximately $30°$ per rotation with a rotation rate close to 2 Hz. Since raw data are acquired at 1250 Hz, the maximum resolution for a single pass is near $3'$. Before a map is generated from this raw data, the data are resectored into 250 optical sectors for each rotation, thereby decreasing the maximum resolution for each resectored data point to $\sim7'$. Since the pointing model is iterated to regenerate Galactic point sources, the maximum resolution of the map necessarily places a limit on pointing reconstruction. Other important limitations are telescope "jitter" and also how well the pixelization scheme aligns with the point sources. These uncertainties degrade by about 15% the inherent angular resolution and provide the final effective FWHM (assumed Gaussian) of $22' \pm 2'$ and $33' \pm 3'$ in the Q band and Ka band, respectively. These effective beam sizes are taken from the final mapped response of the telescope due to point sources in the Galactic plane.

1.3. Receivers

The receivers in the BEAST radiometer are total power receivers (see Fig. 9), with modulation on the sky provided by the rotating flat reflector. The detector array is housed in a cryogenically cooled vacuum vessel with a cylindrical window that allows the incident microwave radiation to enter to the detector array. The window of the Dewar, which is 18 cm in diameter, is composed of a 7 cm thick cylindrical section of polypropylene-based foam.[8] The radiometric temperature of this window at our frequencies was measured at 3.4 K for the Q band and 2.9 K for the Ka band. In order to limit the thermal radiation entering through this same port, we placed an infrared (IR) blocker between the primary vacuum window and the detector array. This IR blocker is a series of very thin, microwave-transparent layers of extruded polystyrene, each of which thermalizes at a temperature between the temperatures of its adjacent layers; the principle is similar to multilayer superinsulation (MLI). This method allows the physical temperature of the polystyrene layer near the detector array to be reasonably close to that of the array, instead of close to the temperature of the Dewar case, thereby limiting the thermal load on the detector array itself.

After the focused radiation passes through the window, it is terminated onto the detector array. The array comprises a total two Ka-band and six Q-band corrugated scalar feed horns (Villa et al. 1997) that feed the input of the cryogenically cooled low-noise amplifiers (LNA). An ortho-mode transducer[9] is mounted to the output of one of the Q-band feeds. The acquisition of both polarizations could, in principle, be used to measure the polarization of incident CMB photons if the sensitivity of the receiver were good enough and the integration time long enough. This was not true for our receiver, and the simultaneous acquisition of both polarizations allowed only systematics tests of spin-synchronous signals. The Q-band LNAs, based on designs generated at NRAO (Pospieszalski et al. 1995), are 38–45 GHz "A" series amplifiers, each of which have an InP HEMT at the input with a gate length and width of 0.1 and 50 μm, respectively. The remaining FETs are a combination of 100 μm gate width GaAs and InP devices. Band-averaged noise temperatures for each of the Q-band LNAs range from 19 to 29 K, and resulting receiver $1/f$ knees are between 45 and 90 Hz (refer to Table 3 below). Similarly, the Ka-band amplifiers are based on a newer NRAO design (Pospieszalski et al. 2000) that provided better stability and sensitivity than the older "A" series Ka-band amplifiers that were in the possession of our group. These Ka-band LNAs demonstrate band-averaged noise temperatures between 20 and 30 K, with resulting receiver $1/f$ knees around 205 Hz. The templates for each of the normalized power spectra

---

[8] PPA30 Propozote® Foam, product data sheet, Zotefoams, Inc., Walton, KY.
[9] Qband OMT 111588, product data sheet, Vertex Microwave Products, Inc. (formerly gammaf), Torrance, CA.

TABLE 2
"Short List" of Primary Elements Used in Back-End Modules

Source	Element
Precision Tube Company....................	Precision Tube Company's coax part number JS50085 lossy coax
TRW Inc. 1995	InP MMIC model number 44LNA1_80 manufactured by TRW
TRW Inc. 1997	InP MMIC model number ALH192C manufactured by TRW
Agilent Technologies	GaAs MMIC model number HMMC-5040 manufactured by Agilent
Skyworks Solutions Inc......................	Alpha Ind. fixed attenuator models number ATN3580-01, -03, and -06
Anritsu Company...............................	Model 75KC50 detector diode manufactured by Anritsu Company

from the different receivers are shown in the receiver summary section below.

The outputs from each of the Q-band amplifiers have been transformed from the original waveguide to a coaxial transmission line for thermal isolation between the Dewar case and the amplifiers themselves. In the case of the Ka-band amplifiers, this transformation was not possible because of physical constraints in the body case itself and so a transition from waveguide to coaxial[10] was affixed to the output of each of the two Ka-band LNAs. The coaxial transmission line chosen[11] has an outer conductor diameter of 0.″085. This geometry prevents higher order moding up to 65 GHz, which is well above our highest frequency. In addition, the outer conductor is made of stainless steel, which is a poor conductor of heat (as well as electricity). To limit the losses due to the poor electrical conductivity of the stainless steel, the inner diameter of the outer conductor is plated with a very thin ($\sim$1 μm) layer of silver—this thickness represents several skin depths at our frequencies. The loss introduced by this coaxial line, between 7 and 10 dB depending on receiver, was sufficient to provide isolation between the output of the cryogenic LNAs and the input of the LNAs in the warm amplification section to prevent oscillations.

The biasing of the cryogenic amplifiers is performed through the use of constant-current bias circuitry. This circuit allows the user to preset the drain bias conditions desired for each of the transistors in the LNAs before connecting to the LNA, and the circuit will servo the gate to the appropriate voltage to achieve the desired drain settings once the amplifier is connected. An additional feature of the bias circuitry is an external voltage input for both gate and drain voltages (if the user deselects the servo mode), which is convenient for generating $I - V$ plots for the FETs.

Warm amplification of the signal exiting the Dewar is accomplished with integrated modules named the "back-ends." These back-end modules are a series of MMIC-based amplifiers followed by level setting attenuation, a bandpass filter, and finally a detector diode. There are three stages of amplification: two InP[12] and one GaAs.[13] The signal is subsequently attenuator[14] level adjusted before the use of a microstrip coupled-line filter to limit the signal contribution to the frequency range with good noise characteristics. Once the signal is terminated on the diode,[15] the output signal is fed into the data acquisition system. See Table 2 for a "short list" of primary elements used in the back-end modules.

2. DATA ACQUISITION

Once the RF signal has been translated into a voltage by the detector diodes and associated load it must be conditioned for storage on the flight computer. This operation is the task of our data acquisition system (DAQ). The DAQ is a custom-made circuit that provides switching between gain levels, integration, linear isolated AC coupling to the flight computer output, and linear isolated DC (pre-AC coupling) output (see Fig. 10). The

[10] RA28KM1AA Adapter (Waveguide to Coax), product data sheet, Waveguide Component Specification and Design Handbook, p DS110A, Continental Microwave & Tool Company, Inc., Exeter, NH.

[11] S50085 CryogenicLossy Cables, product data sheet, Precision Tube Company, Coaxitube® Division, Salisbury, MD.

[12] InP MMIC model number 44LNA1_80, 1995, and InP MMIC model number ALH192C, 1997, manufactured by TRW (Now NGST), Redondo Beach, CA.

[13] Agilent HMMC5040 20–40 GHz Amplifier, product data sheet, Semiconductor Products, Agilent Technologies.

[14] ATN3580 DC to 40 Ghz Fixed Attenuator Pads, product data sheet, Skyworks Solutions, Inc., Woburn, MA.

[15] Anritsu 75KC50 Microwave Detector, product data sheet, Measurement Components and Accessories, Anritsu Company.
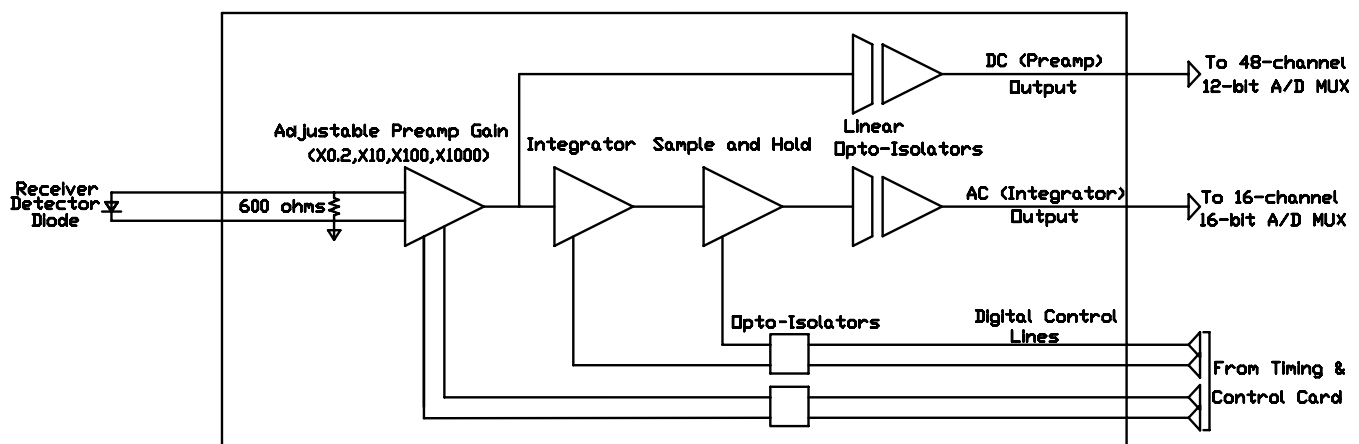

Fig. 10.—Conceptual layout of the DAQ system developed for the BEAST telescope. The signal input to the DAQ is generated by the detector diode at the tail end of a receiver chain, and the two isolated outputs are sent to two separate computers for A/D conversion and subsequent storage.
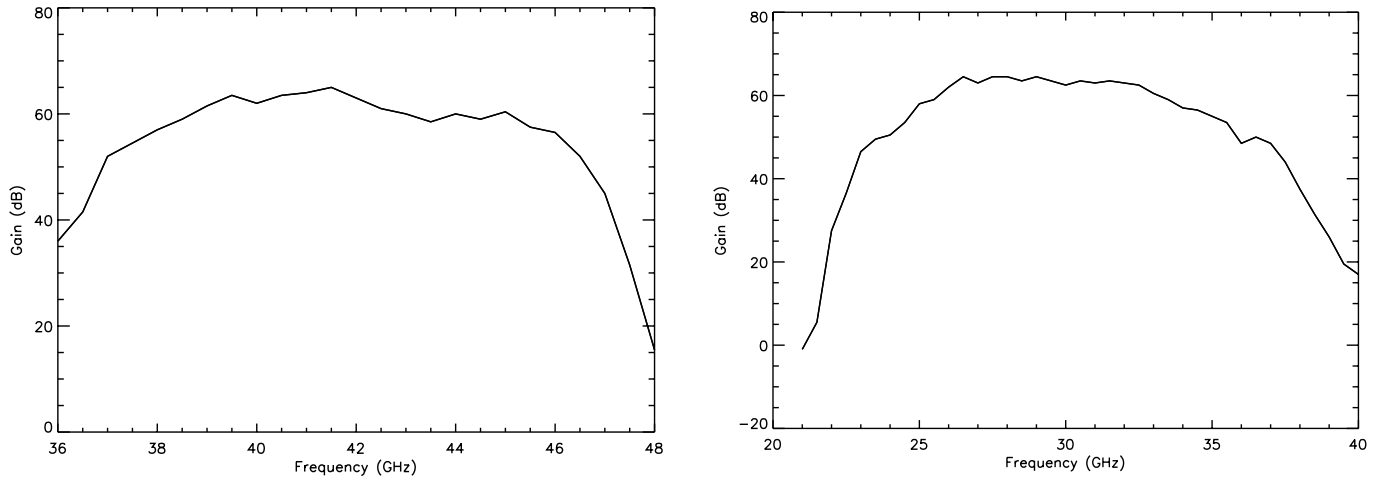
FIG. 11.—Typical Q-band (*left*) and Ka-band (*right*) receiver gain profile, shown with a resolution of 0.5 GHz. The gain drops off rapidly beyond the frequency range of the passband, as shown in the figures.

output to the flight computer is accepted by a 16 bit, 16 channel MUX, and the timing associated with the acquisition from any particular channel is performed by way of a timing control card. Along with an input noise of $\sim$5 nV $\sqrt{\text{Hz}}^{-1}$ the circuit has four levels of DC gain: $\times 0.2$, $\times 10$, $\times 100$, and $\times 1000$. The gain of the AC portion of the DAQ is $\times 80$ at the 1250 Hz acquisition rate that is used by the data acquisition system. Switching between the four possible preamp gain settings is accomplished by digital addressing of two bits that are common to the entire set of DAQ channels (one channel for each radiometer chain). The gain is always chosen to provide the best signal-to-noise ratio while insuring that neither the DC nor the AC portion of the system is ever in saturation while acquiring sky data for map generation.

Although the primary task of the DAQ system is to condition acquired AC signals for storage on the flight computer, it also has an output for the DC signal level at the point just before the signal reaches the AC coupling portion of the circuit. This output is particularly useful for simple diagnostics as well as an immediate check for normal radiometer operation, since there is a DC output for each radiometer channel that is proportional to the gain of that radiometer channel. This DC output data are also saved to computer, and its level allows postacquisition analysis of the signal level for correction to the calibration constant due to diode compression during calibration.

3. RECEIVER PERFORMANCE SUMMARY

The BEAST array can accommodate nine individual receiver chains, but only six were operational at the WMRS at Barcroft Station. Two of the operational receivers operate in the Ka band (from 26 to 36 GHz) and four operate in the Q band (from 38 to 45 GHz). Each of the receivers has an independent feed horn with the exception of two of the Q-band receivers, which accept the two polarization outputs from an ortho-mode transducer attached to a single feed. The typical gain profile in the passband of the Q-band and Ka-band receivers is shown in Figures 11*a* and 11*b*, respectively. The gain drops off quickly ($\sim$10 dB per GHz) on either side of the frequency passband as shown in these figures.

The receivers, used in total power mode, exhibit gain fluctuations and other features that are most easily viewed in frequency space. Figure 12 shows the normalized power spectra

for all six of the receivers used to collect the data at Barcroft Station. The resulting data set used to generate the CMB map (Meinhold et al. 2005) is approximately 625 hr in duration, and this complete (raw) data set was used to generate the spectra shown. There are three dominant features of the spectra in Figure 12, which are the $1/f$ knee, the second harmonic of 60 Hz structure, and finally the harmonics of the flat spin frequency. The $1/f$ knee is defined as the frequency at which the gain fluctuations are equal in power to the white-noise limit of the receiver. The typical knee frequency for the Q-band receivers is approximately 70 Hz; the actual value for each receiver is shown in Table 3 as well as on the power spectra shown in Figure 11. The power spectra have been fit to a $1/f$ model of the form

$$\text{Wnl}[1 + (f_{\text{knee}}/f)^{1.4*\alpha}], \qquad (1)$$

where

$$\begin{aligned} \text{Wnl} &= \text{white noise limit}, \\ f_{\text{knee}} &= 1/f \text{ knee frequency}, \\ f &= \text{frequency}, \\ \alpha &= \text{unitless exponent factor}, \end{aligned}$$

with the resulting values for α placed in Table 3. One feature in the power spectra that is shared by all the receivers is excess power in a region surrounding 120 Hz. The BEAST telescope as a whole is powered by supplies that operate on the normal 60 Hz available from a wall socket. Although filtering was engineered to eliminate the 60 Hz contamination, a small component remained that manifested itself as the second harmonic of the 60 Hz signal. The "width" of this contamination is slightly extended primarily because of beating with the 1.2 Hz frequency component generated by the CTI cryocooler used to cool the array of cryogenic amplifiers.

The last notable common spectral feature is a series of frequency "spikes" in the low frequency ($\leq$10 Hz). These spikes are identified as harmonics of the spin frequency of the rotating flat reflector due to expected modulation of the atmospheric signal seen as BEAST views varying air mass. These spikes are effectively removed by running the raw data through a 10 Hz high-pass filter before map generation. The major features of
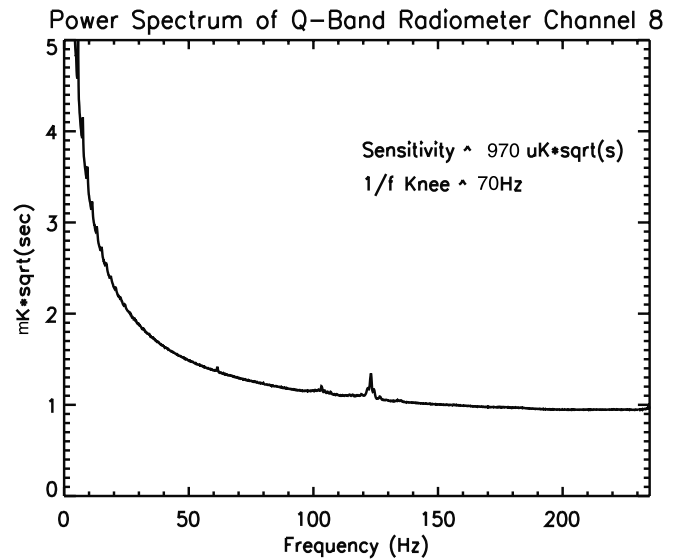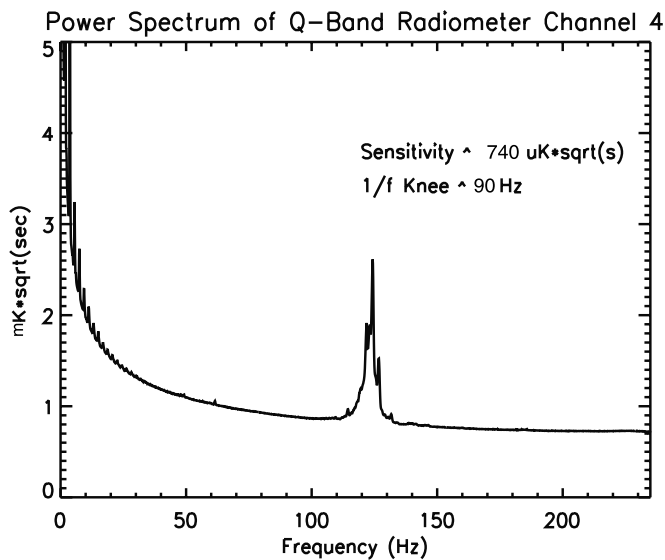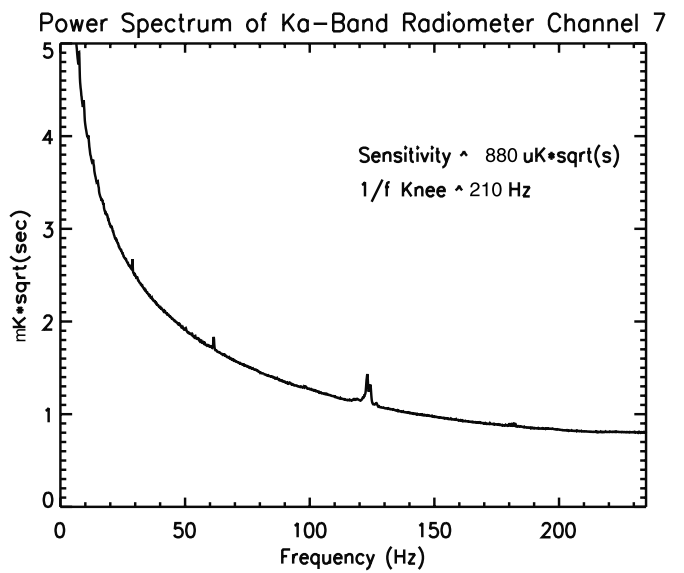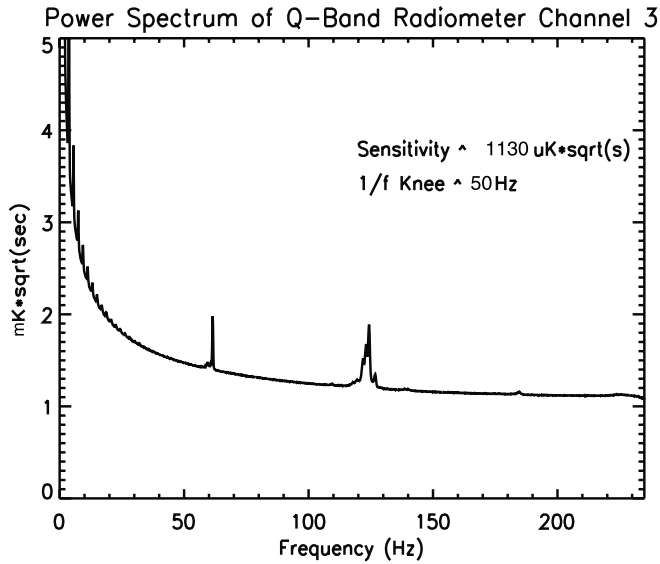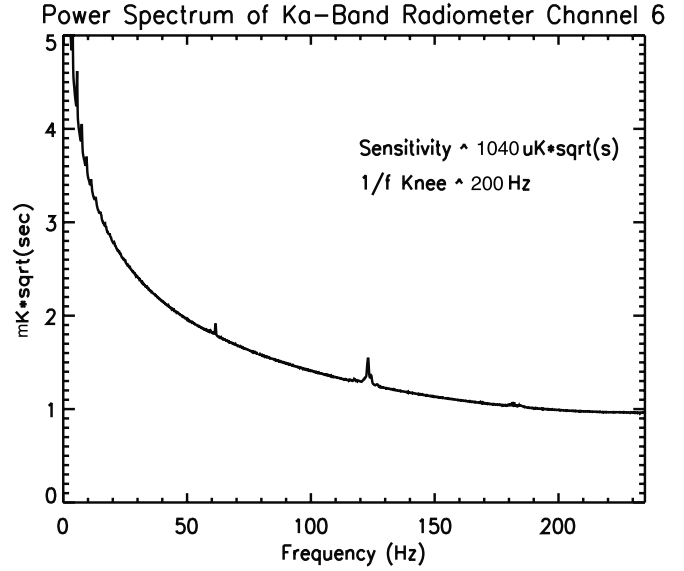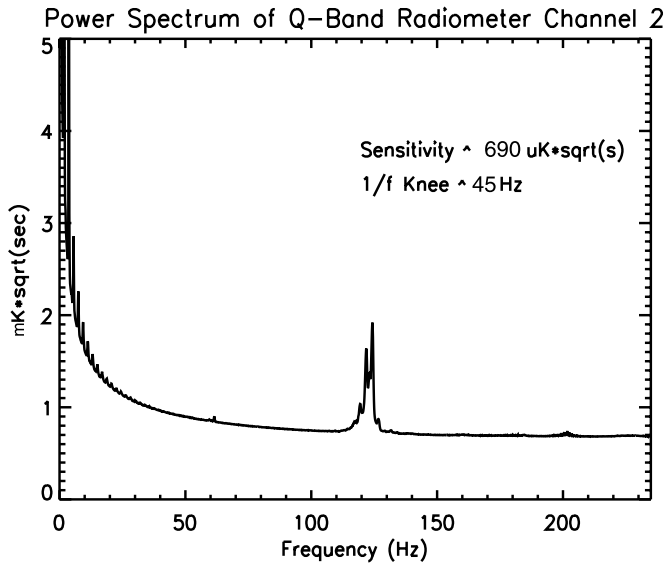
FIG. 12.—Normalized power spectra for the receivers in the BEAST array. All spectra demonstrate $1/f$ characteristics, 120 Hz features, and harmonics of the rotating flat reflector spin frequency.

TABLE 3

SUMMARY OF THE MAJOR CHARACTERISTICS OF THE RECEIVERS USED IN THE BEAST RADIOMETER
AT THE WMRS BARCROFT STATION

Channel Band	WM T_{sys} (K)	WM BW (GHz)	Sensitivity on WM Sky ($\mu K \sqrt{s}$)	α (from $1/f$ model)
2 Q[a] (38–45 GHz)....................	24.3	4.54	690	0.80
3 Q[a] (38–45 GHz)....................	35.8	3.72	1130	0.73
4 Q (38–45 GHz).....................	27.8	4.37	740	0.74
6 Ka (26–36 GHz)	35.6	5.08	1040	0.80
7 Ka (26–36 GHz)	23.1	4.56	880	0.90
8 Q (38–45 GHz).....................	31.0	3.58	970	0.75

[a] Channels 2 and 3 are the two polarization outputs from the single feed attached to the ortho-mode transducer.

the receivers used in the BEAST detector array at the WMRS Barcroft Station are shown in Table 3.

4. CALIBRATION

The microwave data that have been collected have been transformed into voltage data for storage on the computer. In order to translate the voltage map back into a temperature map, a conversion factor must be calculated to multiply with the voltage data. This conversion factor is called the "calibration constant" and has units of K V^{-1}. Measurement of the calibration constant is performed through the use of a calibrator integrated onto the telescope. The calibrator is an ambient load of Eccosorb that is periodically swung into the beam to measure the response of the telescope to a target of a known radiometric temperature. Embedded within the Eccosorb is an ambient-temperature sensor,[16] which feeds back the actual temperature of the load while the calibrator is in the beam. The calibrator is placed in the beam as part of a calibration sequence at the beginning of each hour. This calibration sequence lasts about 5 minutes, during which time four distinct events occur (see Fig. 13). While acquiring data, the gain of the DC portion of the DAQ is set at a gain of ×100. With no change in gain, the calibrator swings into the beam, causing the AC output from the DAQ to temporarily saturate in the positive direction (this is the first event). With no changes in input signal, the AC portion will slowly fall out of saturation with a timescale characteristic

[16] AD590 TwoTerminal IC Temperature Transducer, product data sheet, Analog Devices, Norwood, MA.

of the DAQ circuit (close to 4 s). The AC output is then allowed to decay back to its steady-state level near zero. Next, the gain of the DC portion of the DAQ circuit is switched from ×100 to ×0.2, which saturates the AC portion in the negative direction (the second event). Once the AC part of the circuit has decayed back to zero, the calibrator is removed from the beam, which produces a relatively small negative drop in the AC output of the DAQ; it is from this third event that we extract the calibration constant. The last of the four events is simply switching back to the original gain while viewing the sky.

The purpose of the four events is as follows:

Event 1.—Observe the change in output of the DC portion while on a gain setting that provides sufficient signal-to-noise ratio when we change our target from the sky (near 10 K) to the calibrator (near 270 K).

Event 2.—Switch to a gain setting that will keep the change of the AC output on scale when we move the calibrator out of the beam (and wait for AC circuit to settle).

Event 3.—Observe actual change in AC output when calibrator moves out of the beam.

Event 4.—Return to original gain setting and continue collecting data until the beginning of the next hour.

As previously mentioned, it is from the third event that we calculate the calibration constant. An "exploded view" of the third event is shown in Figure 14. Shown in the TOD of Figure 14 is the stable output at the beginning of the plot that is due to the radiometer viewing the ambient calibrator target at a gain
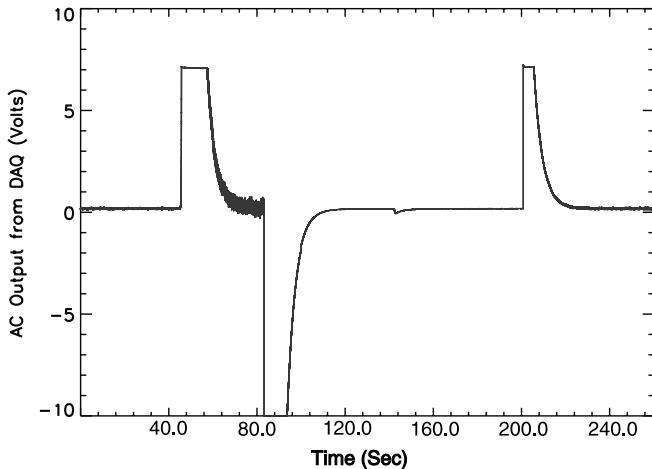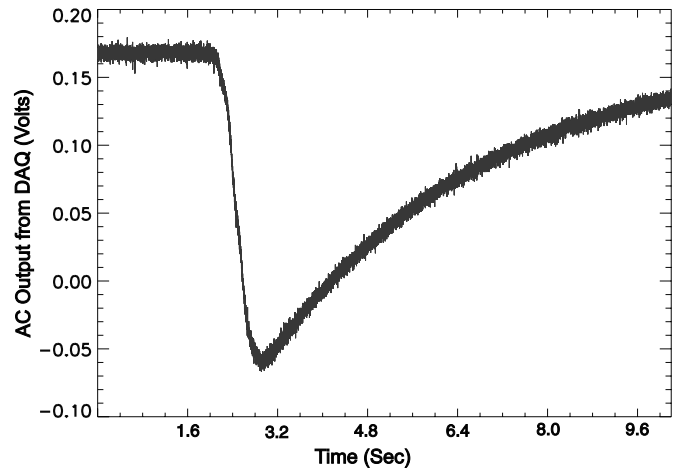

FIG. 13.—Output from data stream during a typical calibration. These calibrations occur at the beginning of every hour and last about 5 minutes. [*See the electronic edition of the Supplement for a color version of this figure.*]

FIG. 14.—"Exploded" view of event number 3 when the gain is set at ×0.2 and the ambient calibration target is removed from the beam returning the view of the sky. [*See the electronic edition of the Supplement for a color version of this figure.*]
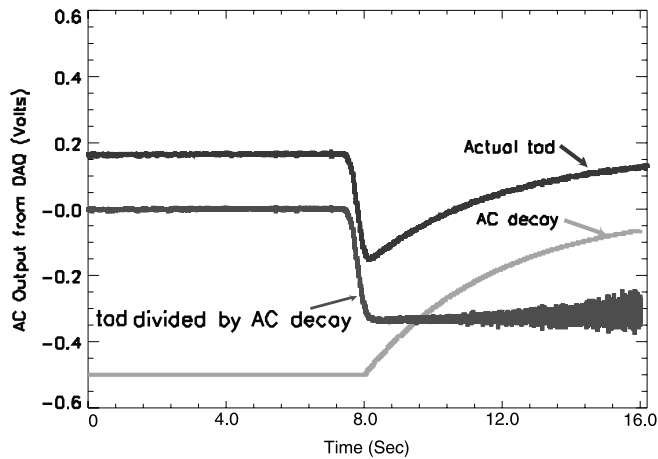
FIG. 15.—Dividing the measured TOD by the AC decay of the DAQ circuit gives the "undecayed" response of the DAQ. [*See the electronic edition of the Supplement for a color version of this figure.*]

of ×0.2. Then, as the calibrator swings out of the beam, the target viewed by the radiometer is the sky (with a temperature of approximately 10 K), which provides a drop in the AC output of the DAQ. Finally, while viewing the essentially constant temperature sky, the AC output decays back toward zero with the ∼4 s time constant of the AC coupling circuit.

The calibrator temperature is measured by a temperature sensor embedded in the ambient target. The approximate radiometric temperature of the sky is 10 K (errors in this value propagate to small errors in the derived constant, discussed below). The ratio of the target temperature change to the measured output voltage change from the DAQ is the calibration constant.

Two nontrivial corrections must be folded into the derivation of the calibration constant that we will apply to the voltage map; corrections from the AC decay of the DAQ itself and from compression of the diode detectors, which are used to convert the RF power into a voltage just prior to the input of the DAQ. The correction to the calibration constant from the AC decay involves two events that have similar characteristic timescales: the motion of the calibrator as it swings out of the beam, and the AC decay of the DAQ circuit. We correct the calibration TOD for both of these effects (see Fig. 15); the voltage swing from this corrected output from the DAQ is used to derive the calibration constant.

The second correction made to the calibration constant accounts for the compression of the diode detectors used to convert the output from the final signal amplifier to the voltage that is directed to the DAQ input. The diodes used on the back-end modules are model number 75KC50 manufactured by Wiltron (now Anritsu Company). An ideal detector diode (appropriately loaded) would output a voltage that is always directly proportional to the signal incident on the diode no matter how large the output voltage becomes. Real detector diodes are limited in how

much current they can source, and sensitive detectors will saturate at rather low signal levels. For the diodes used on the BEAST radiometer, the gain of any particular chain is targeted to output ∼20 mV from the diode when the radiometer is viewing a 300 K target; at this output level, the diodes are outside of their linear regime. Understanding this in advance, we measured the output of each detector diode while varying the input by a known amount to quantify the correction associated with this saturation effect and correct our calibration constants from these data.

Two measurement uncertainties dominate the uncertainty in the derived calibration constant: the calibrator and sky temperatures and the uncertainty in DC gain between gain settings in the DAQ. The results of the primary sources for calibration error are summarized in Table 4. Temperature sensors are used to read out the temperature of the ambient load on the calibrator with an uncertainty of $\pm2^\circ$ C. This $\pm2^\circ$ C corresponds to just under $\pm1\%$ in the derived calibration constants. The uncertainty in the sky temperature plays a nontrivial role in the errors associated with our derived calibration constants. As previously mentioned, the radiometer is presented with an ambient load, whose physical temperature is read directly, as well as the sky to obtain our $T_{\text{calibrator}} - T_{\text{sky}}$ that is used in the derivation of the calibration constant applied to the voltage TOD. The radiometric temperature of the sky is assigned a fixed value of 10 K. The actual sky temperature varies between 8 and 12 K (for the "good" data used) from hour to hour depending on weather conditions. This adds an additional $\pm1\%$ to the error on the derived calibration constants. Since the centroid of the flat reflector points toward zenith, the variable offset generated by the scan is only ∼0.2 K p-p, so errors associated with it are not included.

The second dominant source of error is uncertainty in the gain of the DAQ between different gain scales. The calibration constants are derived on a DAQ gain scale of ×0.2, but the sky data are acquired at a DAQ gain scale of ×100. The calibration constants generated at a gain scale of ×0.2 are applied to the data collected at the ×100 scale, assuming that the gains of these settings are exact. Realistically, the error between these gains could be as large as $\pm3\%$.

System noise folds itself into noise in the actual measure of the calibration constants. There are 682 independent measures of the calibration constant (see Fig. 16) spread evenly across the measured portion of the sky for each receiver. Each of the measures of the calibration constant is applied to the subsequent 55 minutes of the hour during which the calibration constant was measured. The standard deviation in the set of calibration constants of the 682 measures for one receiver is very close to 10%. Since the 682 independent measures are spread evenly across the 24 one-hour intervals, there are 28.4 measures of the calibration constant for any of the 24 one-hour intervals on the sky. This reduces the error bars for any one-hour interval from 10% to slightly less than 2%.

TABLE 4

SUMMARY OF THE PRIMARY CONTRIBUTIONS TO ERRORS IN CALIBRATION CONSTANTS DERIVED ON BEAST TELESCOPE

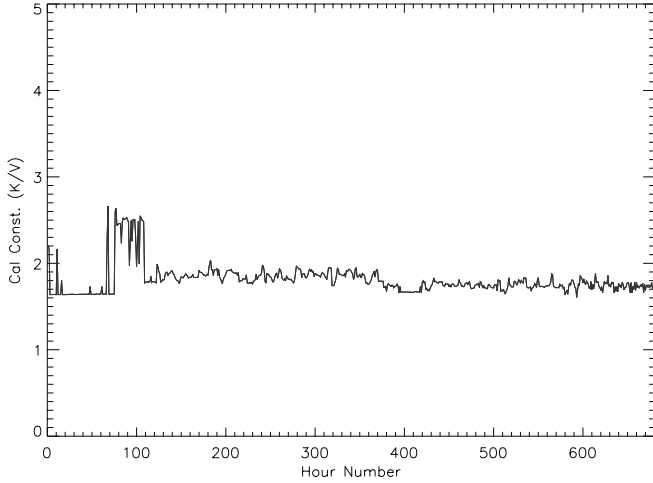| Component	Error Type	Value	Contribution
Temperature sensors..	Absolute temperature readout	$\pm2^\circ$ C	$\pm1\%$
Sky temperature	Absolute	$\pm2^\circ$ C	$\pm1\%$
DAQ..	Gain between DC levels	Estimated	$\pm3\%$
Calibration constant	Statistical noise	Measured	$\pm1\%$
Total			$\pm6\%$

FIG. 16.—Derived calibration constants for all "good" hours used for subsequent map generation. Plateau near hour 100 is due to LEDs (illuminating FETs) being turned off, resulting in lower radiometer gain during that period of data acquisition. [*See the electronic edition of the Supplement for a color version of this figure.*]

Another contributor to our uncertainty in calibration is based on our beam size. The effective beam size (FWHM) obtained by analysis of the final maps is $22' \pm 2'$ in the Q band and $33' \pm 3'$ in the Ka band. This uncertainty manifests itself not by adding error to the calibration constants as they are derived, but rather by adding uncertainty to what we have measured on the sky. This uncertainty is included in the following section regarding the measured flux from Cygnus A.

The calibration procedure described in the previous section is a calibration that occurs between the optics and the receivers. This calibration does not take into account effects associated with optical efficiency, beam efficiency, etc. An important test to ensure that the calibrations generated using the sequence described above are valid for the sky is to compare the flux measured from a source in the sky by the BEAST telescope and compare that to previously reported results for the same object; Cygnus A will be used as the test source. The derivation between incident flux and the antenna temperature is shown, followed by the reported results for the measured flux of Cygnus A. Finally, the measured antenna temperature of Cygnus A by the BEAST experiment is presented, showing a good match with the expected results:

$$SA_e\beta = KT_a\beta, \qquad (2)$$

where

$$S = \text{Flux in W m}^{-2}\text{ Hz}^{-1},$$
$$A_e = \text{effective aperture area},$$
$$\beta = \text{bandwidth},$$
$$k = \text{Boltzmann's constant},$$
$$T_a = \text{antenna temperature},$$

where $T_a = S_{\text{Jy}}A_e/1.38$ mK and S_{Jy} is the flux in Jy.

Using $A_e = \lambda^2/\Omega$, where Ω is the solid angle and λ is the wavelength, and solving for the solid angle assuming Gaussian beam of folding width σ,

$$\Omega = \int e^{-\theta^2/2\sigma^2} \sin^2\theta \, \partial\theta \int e^{-\phi^2/2\sigma^2} \, \partial\phi, \qquad (3)$$

gives

$$\Omega = 2\pi\sigma^2 = (\pi/\ln 2)(\text{FWHM}/2)^2, \qquad (4)$$

where $\text{FWHM} = 2\sigma\sqrt{2\ln 2}$.

For the BEAST telescope in the Q band $\text{FWHM}_Q = 22' \pm 2'$, and in the Ka band, $\text{FWHM}_{\text{Ka}} = 33' \pm 3'$ giving

$$\Omega_Q = 4.6^{+0.9}_{-0.8} \times 10^{-5}\text{ sr},$$
$$\Omega_{\text{Ka}} = 10.4^{+2.0}_{-1.8} \times 10^{-5}\text{ sr}, \qquad (5)$$

and

$$A_{e(Q)} = 0.89 \pm 0.16\text{ m}^2 \text{ for } \lambda_Q = 0.72\text{ cm} \quad (41.5\text{ GHz}),$$
$$A_{e(\text{Ka})} = 1.0 \pm 0.2\text{ m}^2 \text{ for } \lambda_{\text{Ka}} = 1.0\text{ cm} \quad (30.0\text{ GHz}), \quad (6)$$

and finally, for 1 Jy, we get the antenna temperature, in mK (for only one polarization),

$$T_Q = 0.32(\pm 0.06)\text{ mK in Q band},$$
$$T_{\text{Ka}} = 0.38(\pm 0.07)\text{ mK in Ka band}. \qquad (7)$$

In order to have a test of the accuracy in the overall level of the calibration of the detector, we use the flux received from Cygnus A. Taking the absolute spectrum from Cygnus A for the frequency bands covered by the receivers (Baars et al. 1977),

$$\log S_{\text{Jy}} = a + b\log\nu(\text{MHz}) + c\log^2\nu(\text{MHz}), \qquad (8)$$

with

$$a = 7.161 \pm 0.053; \quad b = -1.244 \pm 0.014; \quad c = 0. \quad (9)$$

Integrating this flux across the typical bandpass profiles shown previously in Figures 11*a* and 11*b* and including 3% loss due to atmospheric attenuation gives

$$S_Q = 25.4\text{ Jy}, \quad S_{\text{Ka}} = 38.7\text{ Jy}, \qquad (10)$$

as a weighted average so we should expect $8.2^{+1.6}_{-1.4}$ mK in the Q band and $14.6^{+2.8}_{-2.5}$ mK in the Ka band for 10% effective beam smearing, the quoted beam uncertainty, 3% sky loss, and only one of the two polarizations. We actually measure $9.1(\pm 0.5)$ mK in the Q band and 13.8 (± 0.8) mK in the Ka band, which is shown to be within existing calibration error bars. When we pass across Cygnus A once, we dwell on it for only about 1/180th of a second. With a typical sensitivity of $\sim$750 μK $\sqrt{\text{s}}$ this would generate a measurement with ΔT of $\sim$10 mK, but it also takes about 150 passes for Cygnus A to move through our beam (and Cygnus A crosses the beam scan twice), which reduces the error bars on a daily measurement of Cygnus A to $\sim$600 mK. In addition, we view Cygnus A on 26 days, which places error bars on our measure of the radiometric temperature of Cygnus A $\sim$110 mK. This represents a 2% error in what we report as the flux from Cygnus A (i.e., 9.1 mK in the Q band and 13.8 mK in the Ka band). Collectively, this demonstrates the absolute calibration accuracy of the two Q-band and one Ka-band channels on BEAST that view Cygnus A directly and places high confidence on the absolute calibration of the remaining three channels that do not, since their calibration is derived in exactly the same manner as for the three channels that view Cygnus A. In this way we can use the calibration verification of the three channels that do view Cygnus A as a transfer standard for the three channels that do not. It is also important to note that the power spectrum

Fig. 17.—BEAST telescope housed within the modified storage garage at Barcroft Station near White Mountain, California. A section of the roof was cut from the building and placed on rollers to protect the telescope during poor weather conditions. [*See the electronic edition of the Supplement for a color version of this figure.*]

derived from the resulting BEAST map (O'Dwyer et al. 2005) is consistent with other recent estimates.

5. OBSERVING CAMPAIGNS AND SCIENCE PRODUCTS

The BEAST telescope was originally designed for data acquisition from a balloon-borne stabilized platform near 35 km. These helium-filled balloons are typically launched from several sites in the US (one located at Fort Sumner, New Mexico) by the NASA/NSBF crew. Three ballooning seasons were spent in Fort Sumner, resulting in two flights that began on 2000 May 20 and October 16. The first of the two flights failed when the reflecting surface of our rotating flat reflector delaminated from its honeycomb core, which occurred on ascent. The second flight had a number of different problems, but the flight was only about 5–6 hr at float, and the detector sensitivity, along with our scan, generated pixel error bars that were too great to make a useful CMB map. After these two balloon flights we revisited our strategy for data acquisition. The conservative choice was made to collect data from the ground at a high-altitude site so that any problems that occurred could be remedied and data acquisition could resume without the typical 6 month cycle associated with balloon flights. The WMRS Barcroft Station near White Mountain, California, was selected, and our group annexed one of two storage garages. A section of the roof was cut from the garage and placed on rollers to provide a structure that would both house the BEAST telescope (in a "stripped-down" form) and also allow the roof to be closed in the event of poor weather. The BEAST telescope is shown in Figure 17 assembled inside the garage in the orientation typical for data acquisition. When placed in this observing configuration, the beam is near zenith

and the "front" of the garage where the telescope is housed points 74° from north.

Data acquisition from Barcroft Station began in mid-July of 2001 and continued until early December of 2001, at which time we shut down for the winter because of poor weather conditions. The telescope beam was scanned in elevation from the beginning of the campaign until mid-September, when a problem arose with the elevation drive circuitry; the elevation was then fixed with the centroid (the "center" of the elliptical beam path for the receivers) near zenith. In 2002, approximately 5 more weeks of data, split between the spring and fall, were acquired with the elevation fixed near zenith. All of the useful data that have been selected to generate subsequent CMB maps come from these fixed-elevation data sets. This choice was due primarily to the difficulty of reconstructing the pointing of the beam with additional elevation-dependent optical tilt parameters (i.e., elevation-dependent pitch and roll of the telescope as a whole). Out of these "good" data, cuts were made for weather, system-related problems, data transfer from the telescope's computer, calibrations, etc. In the end, 626 hr of data were used to generate the maps that represent the data.

The final calibrated data sets for the six receivers have been culled and high-passed at 10 Hz. These "good" data then have a pixel number associated with them that corresponds to a HEALPix pixelization scheme with HEALPix parameter NSIDE=512. Once the pixel numbers have been assigned to the data, the maps have been generated using the HEALPix (Gorski et al. 2002) routines.[17] The details associated with the generation of the resulting maps are

---

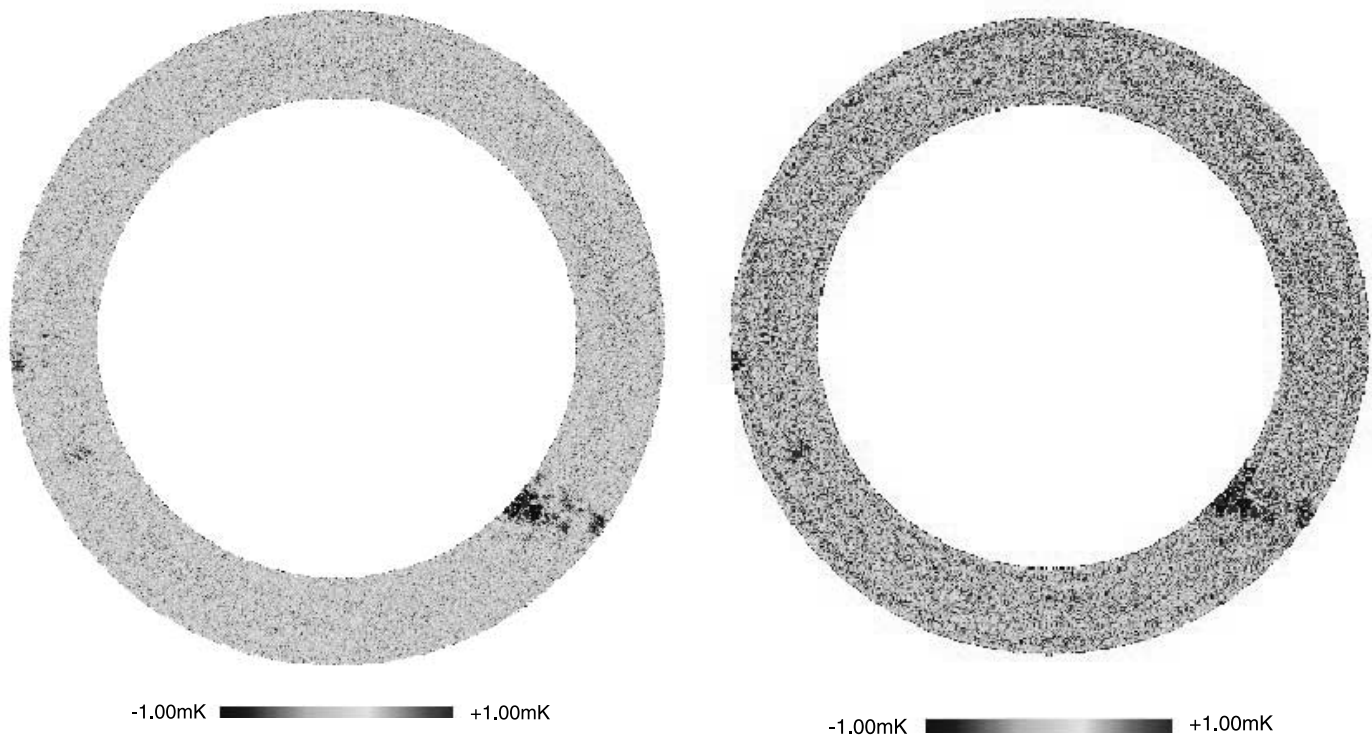[17] Located at http://www.eso.org/science/healpix/routines.

Fig. 18.—Gnomonic projection centered on the north celestial pole of Q-band map with 23′ resolution (*left*) and Ka-band map with 31′ resolution (*right*). The higher pixel noise in the Ka-band map is provided from map generation from the data of only two Ka-band receivers as compared to the map in Q band, which is due to the sum of three receivers (each with better average sensitivity). Dominant features in the lower portion of the maps are due to emission from the Galaxy. [*See the electronic edition of the Supplement for a color version of this figure.*]

discussed completely in a companion paper (Meinhold et al. 2005) and are shown below in Figure 18*a* for the Q-band and Figure 18*b* for the Ka-band receivers. Each of the maps is a gnomonic projection centered on the north celestial pole. Each annulus has an annular width about ±4°.5, a declination of about 37°, and comprises nearly 125,000 pixels each of approximately 7′ size.

The BEAST telescope was designed for optimization of angular power estimation in the *l*-space range from 100 to approximately 500. The angular power spectra extracted from the maps as well as the error bars associated with the estimate (obtained through Monte Carlo simulations) are presented in a companion paper (O'Dwyer et al. 2005). The portion of the map that includes the most emission from the Galaxy (Galactic latitude less than 17°.5) has been omitted prior to the generation of the power spectrum. In addition to the angular power estimation, the cosmological parameter estimates of the BEAST results combined with recent cosmological data are presented in the companion paper.

6. CONCLUSION

The BEAST telescope has been designed and built with the purpose of providing measurements capable of generating a map of CMB anisotropies with ∼20′ resolution. The goal of the map is to allow an estimate of the angular power spectrum associated with the fluctuations from which cosmological parameter estimation can be accomplished. The BEAST telescope utilizes an off-axis Gregorian optical system with receivers that operate in total power mode. Modulation of the beams on the sky is performed through the use of a rotating flat reflector. This scheme offers simplicity in the receivers while providing better intrinsic sensitivity than switching radiometers. This instrument paper has been published in coordination with a paper describing the map generation process (Meinhold et al. 2005), the power spectrum and cosmological parameter estimation (O'Dwyer et al. 2005), the details of the optical design (Figueiredo et al. 2005), and the analysis of the Galactic foreground contribution to the BEAST maps (Mejía et al. 2005).

An instrument description of the BEAST telescope has been included, with a detailed discussion of the receiver properties, calibration methods, and calibration verification on a celestial source. Finally, the resulting data set is briefly described and is used to generate maps of the fluctuations in the CMB. The several-element feed array has achieved good performance owing to the very large size of the BEAST telescope. The achieved system stability, with a ground-based scan strategy and a long-lasting experiment, has allowed the generation of maps with relatively large sky coverage.

REFERENCES

Baars, J. W. M., Genzel, R., Pauliny-Toth, I. I. K., & Witzel, A. 1977, A&A, 61, 99
Dragone, C. 1978, Bell System Tech. J., 57, 2663
Figueiredo, N., et al. 2005, ApJS, 158, 118
Gorski, K. M., Banday, A. J., Hivon, E., & Wandelt, B. D. 2002, ASP Conf. Ser. 281, Astronomical Data Analysis Software and Systems XI, ed. D. A. Bohlender, D. Durand, & T. H. Handley (San Francisco: ASP), 107
Hivon, E., Górski, K. M., Netterfield, C. B., Crill, B. P., Prunet, S., & Hansen, F. 2002, ApJ, 567, 2
Kolb, E. W., & Turner, M. S. 1990, The Early Universe (New York: Addison-Wesley)
Langston, G., Minter, A., D'Addario, L., Eberhardt, K., Koski, K., & Zuber, J. 2000, AJ, 119, 2801
Meinhold, P. R., et al. 2005, ApJS, 158, 101
Mejía J., et al. 2005, ApJS, 158, 109

Mizuguchi, Y., Akagawa, M., & Yokoi, H. 1978, Elec. Commun. Japan, 61-B, 58
Natoli, P. 1998, Ph.D. thesis, Univ. degli Studi di Roma "Tor Vergata"
O'Dwyer, I., et al. 2005, ApJS, 158, 93
Peebles, P. J. E. 1993, Principles of Physical Cosmology (Princeton: Princeton Univ. Press)
Pospieszalski, M. W., Lakatosh, W. J., Nguyen, L. D., Lui, M., Liu, T., Le, M., Thompson, M. A., & Delaney, M. J. 1995, in Proc. 1995 IEEE MTT-S Int. Microwave Symp. Digest, 1121
Pospieszalski, M. W., Wollack, E. J., Bailey, N., Thacker, D., Webber, J., Nguyen, L. D., Le, M., & Lui, M. 2000, in Proc. 2000 IEEE MTT-S Int. Microwave Symp. Digest, 25
Pryor, M. K. 1998, M.S. thesis, Univ. California, Santa Barbara
Staren, J. W. 1999, Ph.D. thesis, Univ. California, Santa Barbara
Villa, F., Bersanelli, M., & Mandolesi, N. 1997, Int. Rep. ITESRE 188/1997
Wandelt, B. D., Hivon, E. F., & Gorski, K. M. 2001, Phys. Rev. D, 64, 083003